



## Using CoCu<sub>2</sub>Ga/SiO<sub>2</sub> to identify stability-issues in ethanol-selective Co-Cu alloyed catalysts in carbon monoxide hydrogenation

Thomas Erik Lyck Smitshuysen<sup>a</sup>, Mads Lützen<sup>b</sup>, Anna Zimina<sup>c</sup>, Thomas L. Sheppard<sup>c</sup>, Helene Hagemann Jakobsen<sup>a</sup>, Ib Chorkendorff<sup>a</sup>, Christian Damsgaard<sup>a,b,\*</sup>

<sup>a</sup> Surface Physics & Catalysis (SurfCat), Department of Physics, Technical University of Denmark, Fysikvej 312, Lyngby DK-2800, Denmark

<sup>b</sup> Nanolab, Technical University of Denmark, Fysikvej 307, Lyngby DK-2800, Denmark

<sup>c</sup> Institute for Chemical Technology and Polymer Chemistry (ITCP), Karlsruhe Institute of Technology (KIT), Karlsruhe 76131, Germany

### ARTICLE INFO

#### Keywords:

CO hydrogenation  
Catalytic alcohol synthesis  
Alloyed nanoparticles  
Material stability  
STEM  
EDX  
In situ characterization  
XRD  
XAS

### ABSTRACT

Hydrogenation of CO to higher alcohols such as ethanol is an attractive pathway for industrial production while avoiding competition with food crops. However, thermocatalytic ethanol production from syngas is currently hindered by the lack of selective catalysts. The structural integrity of ternary-alloyed CoCu<sub>2</sub>Ga nanoparticles supported on silica was studied during thermo-catalytic CO hydrogenation. Catalysts of four different CoCu<sub>2</sub>Ga weight-loadings were tested catalytically under differential conversion, showing their different intrinsic selectivity during CO hydrogenation towards ethanol, methanol, and hydrocarbons. CoCu<sub>2</sub>Ga catalysts with 3.5 wt% and 17.8 wt% proved most and least selective towards ethanol formation, respectively. These two were studied in depth using STEM-EDX of fresh and spent samples showing different size distributions of the nanoparticles for all samples, and a change in the Co/Cu distribution of the nanoparticles from fresh to spent samples. In situ characterization using XRD, XANES, and EXAFS during CO hydrogenation supported the findings of the STEM-EDX and elucidated that the fresh more homogenous catalyst consisting of ternary CoCu<sub>2</sub>Ga nanoparticles de-alloyed into Cu-rich and CoGa-rich nanoparticles. This de-alloying was possibly driven by two factors: the metastable phase of CoCu<sub>2</sub>Ga decreasing its free energy by separating Cu and Co; and the strong interaction between Co and CO further driving a segregation. From a theoretical standpoint, Cu-Co intermetallics present the most selective catalyst to form ethanol over methane and methanol. The experimental findings presented here support the theory, although further efforts are needed to improve structural stability during the catalytic reaction.

### 1. Introduction

The current “climate change crisis” [1,2], in which humanity’s historical pollution of large amounts of greenhouse gases, most notably CO<sub>2</sub> [3,4], have accelerated [5,6] calls for a revolutionized restructuring of our energy infrastructure. This can include exchanging coal, oil and natural gas for renewable electricity and circular economic practises [7–9]. Hydrogen produced by water-electrolysis and electricity-storage in batteries are an integral part of this restructuring. While these two examples can address electricity needs, they cannot be used more generally for energy needs, i.e. synthesis of carbon-based chemicals and fuels. Catalytic conversion of CO<sub>2</sub> to high-value chemicals lying in the “liquids sweet spot” of high energy density fuels such as ethanol [9]

would meet that need. Ethanol is already widely used e.g. as a detergent, cleaning agent, or directly as fuel [10], while global production in 2021 amounted to 27 billion gallons almost exclusively by fermentation of cornstarch and sugar [11]. However, if ethanol and higher alcohols should be used as a general substitute for fuel or precursor for aviation fuels, a scalable and pressurized catalytic conversion route from syngas is desirable over growing and fermenting crops, since the latter competes with land use for food production [12,13]. Where syngas conversion is a very broad term, we will focus on the hydrogenation of CO into higher alcohols, a process we believe is not mature yet due to the lack of sufficiently selective catalysts. Direct conversion of CO<sub>2</sub> (e.g. from flue gas) into ethanol in a single unit-operation is of course more desirable from a plant-design point of view, but as CO<sub>2</sub>-to-ethanol

\* Corresponding author at: Surface Physics & Catalysis (SurfCat), Department of Physics, Technical University of Denmark, Fysikvej 312, Lyngby DK-2800, Denmark.

E-mail address: [cdda@dtu.dk](mailto:cdda@dtu.dk) (C.D. Damsgaard).

<https://doi.org/10.1016/j.apcata.2024.119636>

Received 21 December 2023; Received in revised form 12 February 2024; Accepted 20 February 2024

Available online 21 February 2024

0926-860X/© 2024 The Authors. Published by Elsevier B.V. This is an open access article under the CC BY license (<http://creativecommons.org/licenses/by/4.0/>).

involves C-C coupling it assumably uses CO intermediates in some capacity: through reverse water-gas-shift [14,15] and/or insertion into methanol or formate (formed from CO<sub>2</sub>) [14,16], making the catalyst properties markedly more complex. In broad terms four different classes of heterogenous catalysts perform CO hydrogenation to ethanol [12]: Rh-based catalysts in which morphology [17], support [18,19] and promotion [20–22] change the Rh active site substantially; Mo-based catalysts [12] of sulfides, carbides, oxides and phosphides, all of which also depend on morphology, support and promotion; modified methanol-catalysts which are usually Cu-based and promoted with more reactive metals [23–26] or alkali-metals [25,27–29]; and lastly, modified Fischer-Tropsch catalysts based on Fe [23,29,30] or Co [31–33], such as partially reducible oxides on the interface of Co to tune the selectivity towards oxygenates [33]. When reviewing literature, one will notice that the last two classes have a very significant overlap due to alloys of Cu and Fe/Co. These alloys have interest, as Cu-Fe and Cu-Co intermetallic sites rationally depict the perfect balance between CO-dissociation and CO-hydrogenation, which has been firmly cemented in DFT-studies [34,35]. Cao et al. showed that the (211)-facet of CoCu (L1<sub>0</sub>) lies just in the very narrow optimum of ethanol-selectivity when considering scaling-relations for CO-hydrogenation to methane, methanol and ethanol [35]. Opposite a reaction-pathway going over methanol, there is the direct coupling of two CO by CO-insertion into CH<sub>x</sub>-species; a reaction-pathway which the stepped surface of CoCu theoretically should be unique in catalysing [35]. However, the issue of alloying Co and Cu is difficult since solubility of either in the other is extremely limited [36,37]. Luk et al. [38] used hollow nano-structured carbon tubes and conical fibers as supports to restrict nanoparticle-growth keeping a high dispersion and intimacy of the Fe and Cu, although they do observe separate phases of Cu and Fe [38]. The same group later used zeolite-supported Cu-Fe and improved the conversion of CO with a so-called “hybrid bed” of both zeolite- and carbon-nanofiber supported catalyst [39], with the highest selectivity for C<sub>2+</sub>-alcohols arising from the catalyst-bed packed in tandem. Cao et al. showed direct alloying of Cu and Co through the preparation of a CoCuAl double-layered hydroxide precursor which was then calcined to form CoCuO<sub>2</sub> followed by reduction [40]. Here they claim to have achieved a catalyst with homogenous and uniform CuCo-nanoparticles supported on alumina, demonstrating ~40% selectivity towards higher alcohols at ~50% conversion and stable operation for several days. The introduction of a third alloying metal (a glue so to speak) into the Co-Cu alloy is also a strategy for making an alloy with high Co-Cu intimacy eg. CoCuMo [41], CoCuZn [24], CoCuNb [42], CuCoGa [43] and CoCuMn [44–46]. These have shown varied success in synthesizing homogenous Co-Cu-X alloy, but nonetheless show high selectivities towards higher alcohol synthesis.

Introducing a third element can from a synthesis point-of-view certainly increase the chances of a homogenous alloy or even intermetallic with Co-Cu sites, but at the same time, it also increases the interactions with neighbors in which phase-separation can occur. Furthermore, operating ethanol synthesis catalysts at high CO-conversion is the normal for testing new catalysts, as it shows the performance under relevant conditions, but it also offers an often-overseen alternative explanation to the existence of Co-Cu sites: namely Co and Cu working separately but in tandem.

In this work, the approach of introducing a third metal was used to make a Co-Cu alloy, namely a ternary CoCu<sub>2</sub>Ga, which has negative formation enthalpy compared to metallic Co, Cu and Ga according to the OQMD-database [47,48]. By simple incipient wetness impregnation of nitrate-precursors on porous silica and a single-step reduction at high temperatures, such a catalyst can produce ethanol at close to zero conversion. Characterization data show that reaction conditions drive a phase-segregation of the alloy due to strong interactions between Co and CO; a concern which should be general in the field of Cu-Co alloys when used for CO-hydrogenation, since the thermodynamic nature of these alloys make a phase-separation irreversible for the loaded catalytic bed.

## 2. Methods

### 2.1. Catalyst synthesis

The samples of CoCu<sub>2</sub>Ga/SiO<sub>2</sub> catalysts were prepared by incipient wetness impregnation and subsequent heat-treatment in hydrogen. Four different types of samples were prepared with a CoCu<sub>2</sub>Ga “metal weight-loading” of 1.9 wt%, 3.5 wt%, 17.8 wt% and 40 wt% (where “metal weight-loading” is the sum of Co, Cu and Ga over the sum of the full sample, assuming Co, Cu and Ga being fully metallic and Si being fully oxidized). In a normal procedure, nitrate-salts of 99.99% Cu(II)nitrate-hemipentahydrate (467855, Sigma-Aldrich), 99.999% Co(II)nitrate-hexahydrate (10694, Alfa Aesar), 99.999% Ga(III)nitrate-hydrate (11150, Alfa Aesar) were dissolved in millipore-water. Pellets of SiO<sub>2</sub>(44740, Alfa Aesar, BET area of 244.2 m<sup>2</sup>/g) were ground to powder and sieve-size-selected to 105–210 μm. This powder was impregnated with water-dissolved metallic nitrates in a single impregnation and with a molar-concentration according to the desired weight-loading. The impregnated powder was dried in a ceramic bowl on a hot-plate set on 120°C for two hours. These powder-samples are referred to as precursor samples. Precursor samples were kept in a ventilated cupboard at ambient conditions. The catalysts were synthesized from the precursor samples in a quartz-glass (ID of 9 mm) plug-flow reactor with 100 ml/min of 90% H<sub>2</sub> in Ar at 1 bar and 620°C. These conditions were kept for 10 hours. SiC was used to dilute the samples giving a bed-length of >20 mm, so they could be packed with the same volume (resultantly using more SiC for higher metal weight loadings to compensate the increased density). Samples undergone the reduction treatment is referred to as “fresh”.

### 2.2. Catalytic tests

Catalysts samples were prepared with a nominal final CoCu<sub>2</sub>Ga metal weight-loading of Co+Cu+Ga being 1.9 wt%, 3.5 wt%, 17.8 wt% and 40 wt%. Samples were quantified using SEM-EDX, whose results are shown in Table S1 and S2. For a test, a precursor sample was loaded in quartz-glass reactor and reduced at 620°C for 10 hrs in 90% H<sub>2</sub> in Ar at 100 ml/min and 1 bar. Hereafter reaction-conditions was imposed on the catalyst. Catalytic tests were performed at 2 bar in H<sub>2</sub> and CO in 2:1, and with trace amounts of Ar. During catalytic tests, the flow was matched to the metal-weight in the catalyst, resulting in weight hourly space velocity (WHSV) of  $130000 \frac{\text{ml}}{\text{h}_{\text{Co+Cu+Ga}}}$  and gas hourly space velocity (GHSV) of 8000 h<sup>-1</sup> (using SiC as filler to keep a constant bed-volume across different samples). Temperatures were cycled stepwise of 15°C between 115°C and 350°C with 1.5 hour of constant temperature before changing. Measurements were taken every 15 minutes, and first point after a temperature-change was disregarded; giving five measurements per reaction temperature. Selectivity is based on the last point before changing temperature. Gas-composition is measured downstream from the reactor using an on-line sampling gas chromatograph (7890 s, Agilent Tech.). Hydrocarbons were retained through a HP-5 column with He as carrier gas and measured on a flame-ionization detector (with a methane sensitivity of >1 ppm). All other gasses were retained through a system of three columns with He as carrier and a thermal conductivity detector. The columns used were HayeSep Q 80/100, HP-PlotQ 40μm and a HP-Plot Molesieve 25μm, and a by-pass to prevent CO<sub>2</sub> and H<sub>2</sub>O from entering the Molesieve column. The linear regression used for calibrating the gas chromatograph gives rise to a relative error of ~1% of the measured value.

Error arising on the selectivity following error-propagation [49] and a 1% relative error on each specie from the gas chromatograph is  $\sqrt{9 * (1\%)^2} = 3\%$  of relative error, eg 8% ethanol ±0.24% (8%\*3%).

### 2.3. SEM-EDX

Scanning electron microscopy with energy dispersive X-ray spectroscopy was used for quantifying the atomic composition of the catalytic grains (105–210  $\mu\text{m}$ ). Samples were exposed to air and mounted on aluminum stubs with carbon-tape by lightly touching the powder with the taped top of the stub. Microscopy was performed either on a Quanta FEG 250 (FEI) with an 80 mm<sup>2</sup> X-Max silicon drift detector (Oxford Instruments) or a Quanta FEG 200 (FEI) with a 50 mm<sup>2</sup> X-Max silicon drift detector (Oxford Instruments). The SEM was operated at 30 keV and the current was optimized towards a dead-time on the EDX-detectors of 20–30%. The Everhart-Thornley detector was used for imaging the sample operating with a grid-voltage of +250 V. The procedure was to scan the beam well within a single grain for 30–120 seconds until the EDX spectrum was converged. With 30 keV the interaction volume is of the size of a few microns [50]. The quantification was done using the manufacturer calibration within the Aztec Software (Oxford Instr.). In the quantification, X-rays arising from oxygen was disregarded, and X-rays coming from Si was assumed to originate from SiO<sub>2</sub>.

### 2.4. STEM-EDX and HR-TEM

High-resolution and scanning transmission electron microscopy with energy dispersive X-ray spectroscopy was performed, where two sets of samples were tested: samples undergone reduction in H<sub>2</sub> and catalytic tests (coined as “spent”); and samples only undergoing reduction (coined as “fresh”). Samples were prepared on a 300-mesh Au lacey-carbon grids (AGS166A3, Agar Sci.) by dropping the grid into the catalytic powder sample, retrieve the grid and shake it gently to remove excess powder. The microscopy was performed on a TITAN 80–300 ETEM X-FEG (FEI) operated at 300 keV and a double tilt Be-holder (Gatan) was used for the microscopy to reduce EDX-background. STEM-HAADF images were acquired with a probe-current of 60–70 pA, scanning with a dwell-time of 12  $\mu\text{s}$  and a camera-length of 300 mm. Beam was blanked between image-acquisitions. EDX was measured at a tilt-angle of 24°–25° and sampled with a X-Max 80 T SDD X-ray detector (Oxford Instruments). Size-distributions were based on STEM-HAADF. ImageJ in the Fiji distribution [51,52] was used to measure the nanoparticle-sizes. In a single measurement a particle was out-lined by the cursor and an ellipse was fitted to this out-line to extract a minor, a major and an average diameter of said particle. The average diameter was used with the assumption that the nanoparticle is spherical. Atomic composition was based on STEM-EDX using the beam to scan within a single nanoparticle. EDX-spectra were acquired by scanning within a nanoparticle for 30 s, while collecting with the EDX-detector; STEM-HAADF images for visual analysis were always acquired prior to collecting EDX-spectra. Cobalt-artifactual concentration in the EDX-spectrum coming from the pole-piece could not be eliminated completely by tilting the sample. Instead, Cobalt was corrected by the measured Fe in the spectrum (only arising from the pole-piece), based on a measurement of the edge of an empty grid performed at the same parameters.

### 2.5. In situ XRD

Precursor samples of 3.5 wt% and 17.8 wt% CoCu<sub>2</sub>Ga/SiO<sub>2</sub> were subject to reduction and catalytic tests while measuring the crystalline phase using powder x-ray diffraction. The apparatus used was an XRK 900 furnace (Anton Paar) with Be-windows situated inside a X’pert Pro XRD (Malvern Panalytical). Samples were pressed onto a Macor ceramic holder with a spatula to create a smooth surface for the XRD. Gas is introduced in a volume above the sample and passed through the sample and the ceramic holder making a flow similar to a plug-flow. Experiments were performed at 1 bar and using gas-compositions as according to the catalyst synthesis and catalytic tests. For the 17.8 wt% sample, the

WHSV was 130000  $\frac{\text{ml}}{\text{hg}_{\text{Co+Cu+Ga}}}$ , whereas for the 3.5 wt% the flow was situationally higher, 660000  $\frac{\text{ml}}{\text{hg}_{\text{Co+Cu+Ga}}}$ , due to the limitations of the equipment and the XRD. The reaction conditions performed in the XRD are at lower pressure than the conditions of the catalytic tests, however the observed materials dynamics are still valid for the analysis as they are supported by several other methods.

The downstream gas-composition was monitored using a QMS (Pfeiffer) and a quartz capillary sniffer. The X’pert Pro XRD (Malvern Panalytical) was equipped with a Ni-filtered Cu K $\alpha$ -anode on the incident-beam and a graphite-monochromator on the diffracted beam. All angle-scans are performed at least twice to make sure that the diffraction pattern is not changing during scans. The XRD-patterns were fitted using Pseudo-Voigt distributions where the peak-position and intensity-ratio between peaks has been fitted according to the recognized mono-atomic crystal structure. Peak-width of the Lorentzian part was fitted and assumed to arise from Scherrer broadening [53] where the peak-width of the Gaussian part was kept constant according to the instrument broadening measured on a Si reference crystal. A background of the XRD-pattern has been established by a “rolling ball”-background [54]. The fitting-model is further explained in SI – *Specifics of the XRD fitting model*.

### 2.6. In situ XAS

Precursor samples of 3.5 wt% and 17.8 wt% CoCu<sub>2</sub>Ga/SiO<sub>2</sub>, and prepared reference samples of 17.8 wt% CuGa/SiO<sub>2</sub> and CoGa/SiO<sub>2</sub>; were subject to reduction and catalytic tests while measuring the X-ray absorption using synchrotron radiation. The samples were prepared with a 9 mm bed within a 1.5 mm OD capillary with 10  $\mu\text{m}$  wall-thickness and mounted in a steel-frame with tube-fittings using epoxy. The epoxy also works as a gas-tight sealing. Samples with 17.8 wt% were diluted with BN to reduce beam attenuation. The capillary was heated with a heat-blower (Oxford Instruments) and the sample-temperature was taken as the average of the temperatures measured just above and below the capillary using a portable type K thermocouple. The gas-system was built on site and a QMS (Pfeiffer Vacuum Thermostat) was used to monitor gasses downstream of the capillary, and to diagnose leakage. The catalysts precursor samples were reduced in 100% H<sub>2</sub> at 1 bar and 620°C for 10 hours and treated in reaction conditions of 67% H<sub>2</sub> and 33% CO at 2 bar at 250°C and 300°C. The gas-flow was set to 8000 h<sup>-1</sup> GHSV according to the bed-volume. “Reference samples” were reduced 100% H<sub>2</sub> at 1 bar and 620°C for 4 hours. Experiments were conducted at the CAT-ACT beamline [55] at KIT Light Source. Absorption was measured in transmission and fluorescence mode of the Co K and Cu K edges upto a wave-number  $k = 16 \text{ \AA}^{-1}$ , and the Ga K upto  $k = \sim 10 \text{ \AA}^{-1}$ . Cu-foil, Co-foil and Ga<sub>2</sub>O<sub>3</sub>-pellet were used –for energy calibration. XANES-acquisition (continues scans) was performed during *in situ* experiments, and EXAFS (step scans) were performed in between individual heating steps, always at 200°C and in the gas-flow of the latest treatment. Data was calibrated, background subtracted and normalized using Athena [56].

## 3. Results and discussion

### 3.1. Catalytic properties for CoCu<sub>2</sub>Ga/SiO<sub>2</sub> in a reaction of CO and H<sub>2</sub>

The catalytic properties of the four synthesized samples of CoCu<sub>2</sub>Ga/SiO<sub>2</sub> (with between 1.9% and 40.0% weight percent of metallic alloy) are shown in Fig. 1. To make the data more legible, only catalytic activity acquired at between 245°C and 335°C are shown to make the differences more apparent (with the rest shown in Figure S1); At below this range the catalysts show very little activity, and above they almost entirely produce methane with minor constituents of C<sub>2+</sub>-hydrocarbons. Fig. 1A show selectivities, where the minor products of DME and C<sub>2+</sub>-hydrocarbons are also visible. For the catalytic activity shown in Fig. 1B,

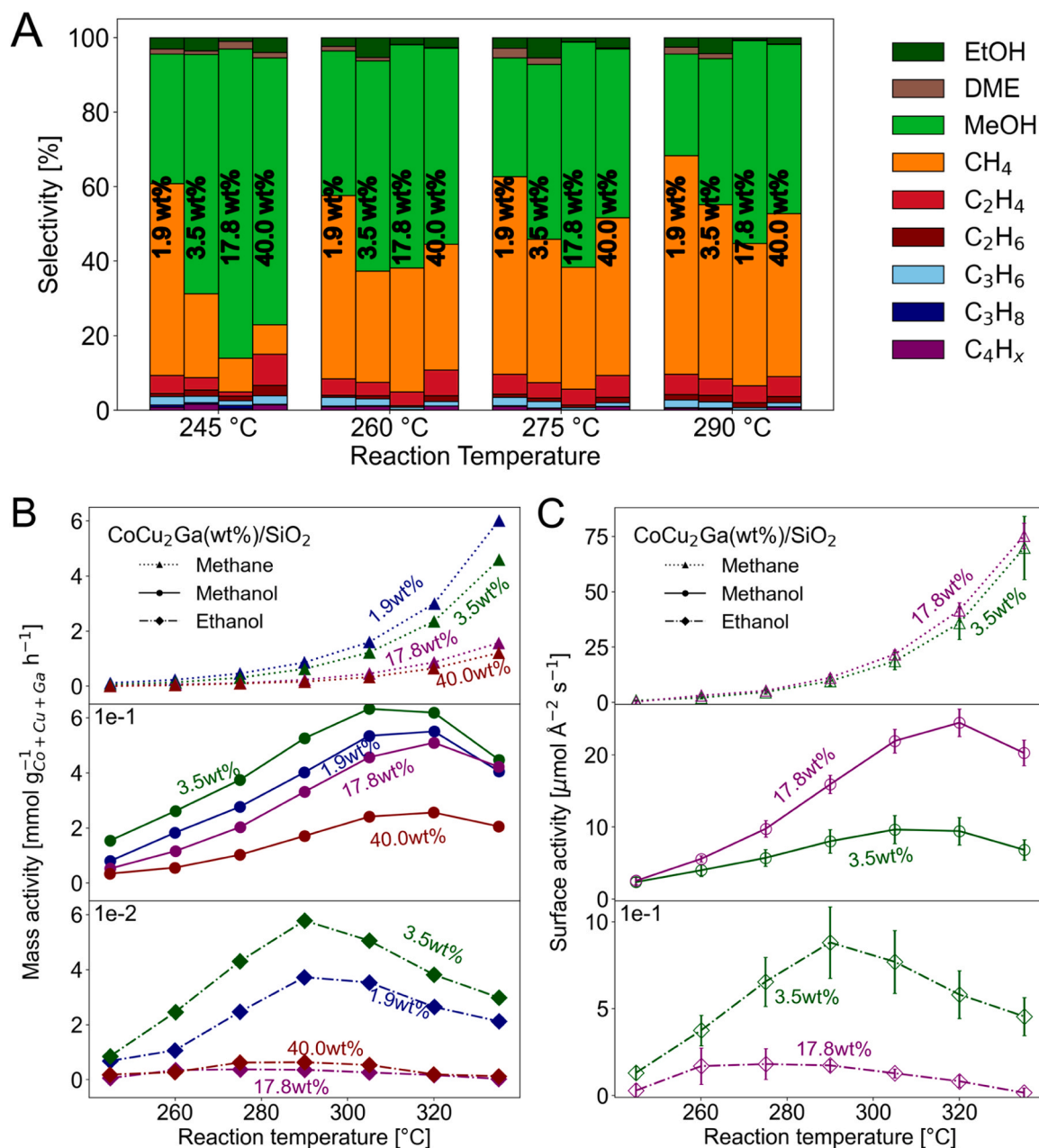


**Fig. 1.** Catalytic tests of CoCu<sub>2</sub>Ga/SiO<sub>2</sub> measured at 245 °C to 335 °C (Full data-set from 125 °C to 350 °C is shown in Fig. S1) with 1.5 hours at each temperature-step, 2 bar, H<sub>2</sub>:CO in 2:1, 100 sccm, 130000 ml/h  $g_{\text{active metal}}$ . Gasses analysed with on-line gas chromatography. All samples are tested, so the same mass of Co, Cu and Ga is present. Gas hourly space velocity was kept high to have a minimal conversion of CO, which at 350 °C was highest and below 0.6%. (A): Selectivity of CoCu<sub>2</sub>Ga/SiO<sub>2</sub>. (B): Mass activity towards methane, methanol, ethanol at 245 °C to 335 °C. (C): Surface-specific activity of methane, methanol and ethanol for 3.5 wt% and 17.8 wt% CoCu<sub>2</sub>Ga. Surface-activity is derived from the crystallite-size shown in Fig. 5B.

it is assumed that the alloyed part of the catalyst, CoCu<sub>2</sub>Ga, is responsible and therefore normalized by that mass (referred to as *mass activity*), and mass activity towards methane, methanol and ethanol is shown per reaction temperature.

All the produced catalysts are similar producing dominantly either methane or methanol with a switch in selectivity at 260–275 °C. At above 275 °C, the mass activity is ordered so the lower weight loading gains higher activity and oppositely for the higher weight loading, i.e. the more active catalysts had lower weight loading of metals. At lower reaction temperatures, where methanol is produced in larger quantities, the weight loading of 3.5 wt% comes out on top producing most methanol and ethanol of all the samples. Above 335 °C, all the catalysts end up producing equal amounts of methanol as thermodynamic

equilibrium is reached. This mechanism is different for methanol opposed to eg. ethanol or methane, as the released enthalpy from methanol synthesis is much lower than ethanol and methane synthesis. The equilibrium limit of methane and ethanol synthesis therefore did not become relevant in the performed experiments.

In terms of ethanol, which Co-Cu alloys are well-known for producing from a theoretical aspect [34,35] and on an experimental aspect [24,40–46], only the CoCu<sub>2</sub>Ga/SiO<sub>2</sub> with 3.5 wt% and 1.9 wt% produce a noteworthy amount. At most, the 3.5 wt% sample achieves 8% selectivity towards ethanol at 275 °C. This is by no means a competitive result compared to other experimental works on Co/Cu/Fe alloys for higher alcohols, though it is not expected to be, as the pressure is very low in the presented experiments and the conversion is insignificant (far



below 0.1% at 275°C). It is however a very positive result at these conditions as it alludes to the existence of Co-Cu even though these two elements are inherently hard to alloy [36]; an existence supported by the materials characterization shown in Section 3.3. Furthermore, when approaching zero conversion, the tandem-effect, where pure Cu produces methanol and pure Co inserts carbon from CO into methanol to form ethanol, is suppressed as very little methanol is present. The fact that the ethanol-turnover peak is before the methanol hints that the methanol is not an important intermediate in these experiments. Opposite the methanol-pathway, the stepped surface of CoCu should catalyze the direct coupling of two closely adsorbed CO [35]. Their selectivity at zero conversion is only 60–70% towards ethanol on their steps and close to 0% on their terraces at 20 bar, according to DFT [34, 35]. For nanoparticles in sizes of ~6 nm, an order of magnitude higher methanol-selective terraces than ethanol-selective edges and corners are present [57]; therefore, it should not be expected that perfectly alloyed and non-promoted nanoparticles would produce more ethanol than methanol at the tested conditions than what is observed in the current work.

From the catalytic experiments, the catalysts producing the most and the least ethanol (CoCu<sub>2</sub>Ga/SiO<sub>2</sub> with 3.5 wt% and 17.8 wt% of metal loading) were selected for further characterization as discussed below. Fig. 1C shows the surface-normalized catalytic activity of the 3.5 wt% and 17.8 wt% sample, based on crystallite-sizes from Fig. 4(right) measured using XRD. Where the 3.5 wt% performed much better in mass activity overall than the 17.8 wt% when normalized by mass, the difference decreases when normalized by surface area. This is even more evident at higher temperatures, when methane-production dominates that the surface activity follows the same slope showing that the intrinsic activity of the two catalysts are similar. This confirms the differential conditions. Furthermore, it shows that the higher metal-loading gives less surface per metal-alloy. A simple relation usually followed from the higher surface-concentration of metallic species giving larger particles and smaller surface per density therefor. In terms of alcohols, the largest difference is noticed, as the larger nanoparticles of the 17.8 wt% produce more methanol, where the 3.5 wt% produce half, but at the same time produce ethanol. This difference must appear from the different distribution of surface sites, when changing the morphology from large to small particles. This is discussed further in Section 3.4.

### 3.2. Stability based on catalytic properties

Fig. 2 shows the catalytic tests of 3.5 wt% CoCu<sub>2</sub>Ga/SiO<sub>2</sub> having repeated the temperature ramp up, showing any changes to the catalytic

performance over time. On the total performance shown in Fig. 2B, there is a substantial change in converted gas, on the second test-cycle, although the production of methanol is barely unchanged. Believing the fall in activity was due to coking, the catalyst was tried re-activated by repeating the reduction-step that formed the original catalyst. As Fig. 2 shows, this reduces both the methanol activity and the total activity; leaving change in morphology as the probable cause. Coke did leave the surface as methane during reactivation as Figure S2 shows, although this did not make the catalyst regain its “fresh” catalytic performance. Cycling the temperature of the 17.8 wt% improved the catalytic performance slightly in terms of more methanol, as Figure S3 shows. Again, change in the morphology is the proposed cause, as will be shown in Section 3.4.

### 3.3. Characterization of the ternary alloy of fresh and spent catalyst

The two catalysts, 3.5 wt% and 17.8 wt% CoCu<sub>2</sub>Ga/SiO<sub>2</sub>, was examined using *ex situ* transmission electron microscopy: a batch of “fresh” samples taken out directly after reduction in H<sub>2</sub>, and “spent” samples taken out after catalytic tests in CO and H<sub>2</sub>. The most important result from this analysis is the size-distributions and chemical compositions of the single nanoparticles measured by STEM-EDX, but a brief summary of the microscopy is given prior. Fig. 3A-C shows excerpt of the microscopy, with more data shown in Figure S4-S6. From the HR-TEM, for both fresh and spent samples of both catalysts, crystalline nanoparticles were found on the SiO<sub>2</sub>-support with fringes of 2.1 Å and 1.8 Å spacing, which fit (111) and (200) of Cu-FCC (Coll. Code: 53755) [58]. Examples of particles were found containing multiple crystallites in the spent catalysts, shown in Fig. 3A and S5. A couple of EDX-linescans of single nanoparticles were performed in all samples, showing all three chemical species of Co, Cu and Ga. Here, it was also observed that a single nanoparticle could hold multiple different phases of Cu<sub>x</sub>Co<sub>y</sub>Ga<sub>z</sub> as Figure S6 shows. These visual observations show that Co and Cu will alloy into nanoparticles even with an incipient-wetness synthesis, where the only driving force is “chemical glue” in the form of Ga and the minimization of surface. We find that the nanoparticles do resemble a ternary alloy.

The size-distribution and EDX-analysis of the single nanoparticles in Fig. 3D and E, substantiate the claim of a ternary alloy. Furthermore other trends appear: the size-distribution moves from larger to smaller nanoparticles going from fresh to spent. This is surprising because it excludes sintering of the ternary alloyed nanoparticles as a deactivation mechanism. For the EDX-concentrations of the 3.5 wt% catalyst shown in Fig. 3D, Co and Cu concentrations goes opposite with small particles

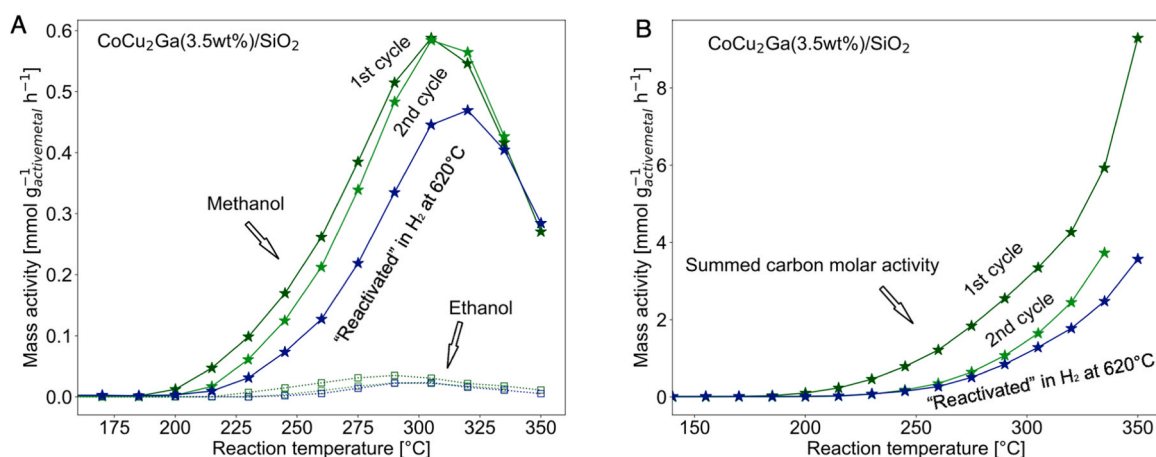
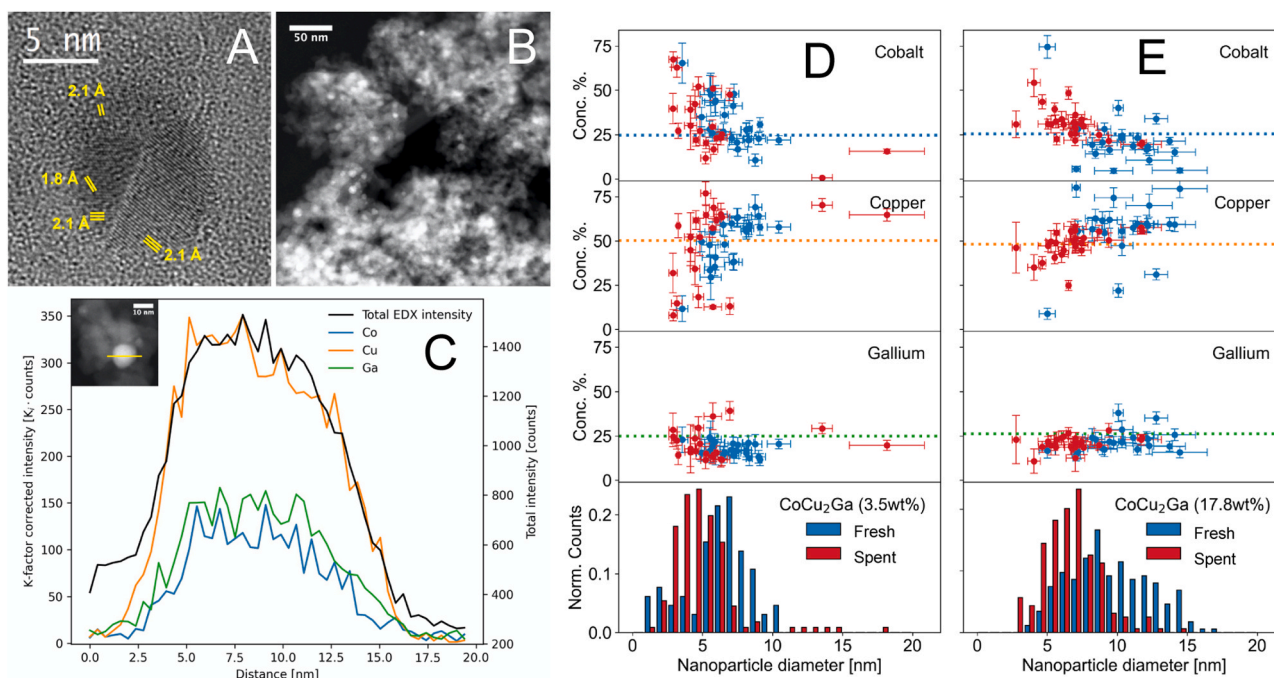


Fig. 2. The effect of cycling the temperature multiple times and “re-activation”. Re-activation procedure was a repetition of the original reduction being 10 hours in 90% H<sub>2</sub>/Ar at 620 °C. Catalytic tests of 3.5 wt% CoCu<sub>2</sub>Ga/SiO<sub>2</sub> measured upto 335 °C with 1.5 hours at each temperature-step, 2 bar, H<sub>2</sub>:CO in 2:1, 100 sccm, 130000 ml/h g<sub>active metal</sub><sup>-1</sup>. Gasses analysed with on-line gas chromatography. Gas hourly space velocity was kept high to have a minimal conversion of CO, which at 350 °C was highest and below 0.6%. (A): Mass activity towards methanol and ethanol. (B): Mass activity based on sum of carbon moles converted.



**Fig. 3.** TEM characterization of  $\text{CoCu}_2\text{Ga}/\text{SiO}_2$  after synthesis (fresh) and after catalytic tests (spent). Samples have been exposed to atmospheric conditions during preparation for the microscopy. More data is available in Fig. S4-S6. (A): HRTEM of spent 17.8 wt%  $\text{CoCu}_2\text{Ga}/\text{SiO}_2$ , and annotated observed fringes. (B): STEM-HAADF of fresh 3.5 wt%  $\text{CoCu}_2\text{Ga}/\text{SiO}_2$ . (C): STEM-EDX line-scan of nanoparticle from fresh 17.8 wt%  $\text{CoCu}_2\text{Ga}/\text{SiO}_2$ . (D): Size-distribution and EDX-quantification of single nanoparticles from 3.5 wt%  $\text{CoCu}_2\text{Ga}/\text{SiO}_2$  based on STEM-EDX for the fresh (blue) and spent (red) samples. (E): Size-distribution and EDX-quantification of single nanoparticles from 17.8 wt%  $\text{CoCu}_2\text{Ga}/\text{SiO}_2$  based on STEM-EDX for the fresh (blue) and spent (red) samples. Dotted lines show the global concentration of Co, Cu and Ga based on the average of the grains in the catalysts powder as determined by SEM-EDX.

being Co-rich where larger ones are Cu-rich. This size-composition relationship is also present for the spent sample of 17.8 wt% but not for the fresh one, as seen in Fig. 3E. This means such relationship was imposed by the CO-hydrogenation reaction for the 17.8 wt% sample: small Co-rich particles have segregated out of the Cu “host” due to the strong interaction of Co to CO compared to that of Cu or Ga. When the same size-composition-relationship is always visible for the 3.5 wt%

catalyst, it must be due to the second driving-force for phase-segregation: the low stability of the ternary alloy. With the lower weight-loading there is less to gain from lowering the surface/bulk ratio, and the formation of the nanoparticles ends up being towards Cu and  $\text{Co}_x\text{Ga}_y$ , which also explains Ga-concentration follows the same trend as Co in 3.5 wt%. In the 3.5 wt% catalyst, the Cu are as larger particles from the initial formation due to the higher mobility of Cu and resulting

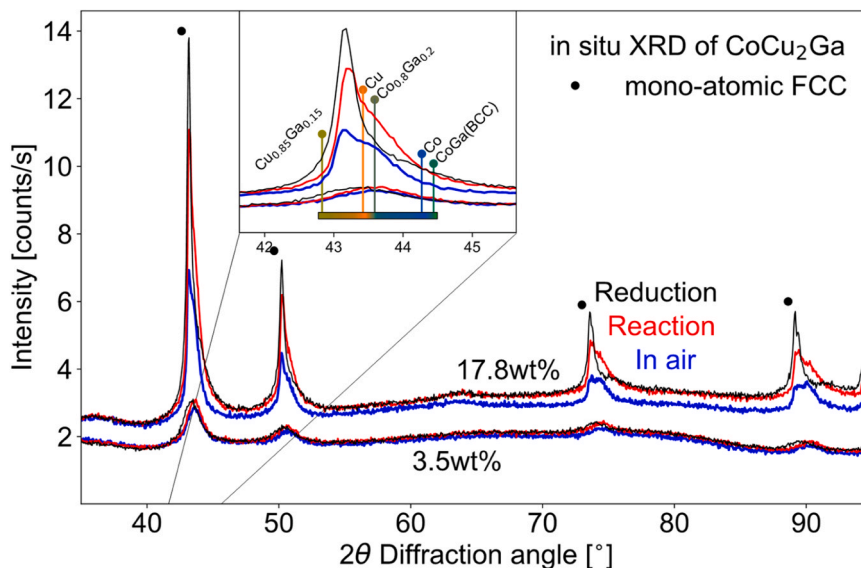


**Fig. 4.** XRD in controlled atmosphere and temperature of 3.5 wt% and 17.8 wt%  $\text{CoCu}_2\text{Ga}/\text{SiO}_2$  after being exposed to reduction conditions, reaction conditions and lastly ambient air at room temperature, all at 1000–1040 mbar. “●” denote a mono-atomic FCC. The in-set plot shows a zoom-in of the main-peak with annotated main-peak-positions of different alloys and intermetallics from ICSD [58] (Coll. Code):  $\text{Cu}_{0.85}\text{Ga}_{0.15}$  (102892), Cu (53755),  $\text{Co}_{0.8}\text{Ga}_{0.2}$  (102426), Co (44989),  $\text{CoGa}$  (102423). They all resemble an FCC crystal-structure except for  $\text{CoGa}$ , which is in a BCC-like structure. The color-bar shows qualitatively, where the peak-position will be situated, depending on the concentration of copper, cobalt and gallium.

sintering. For all samples there is a small deficiency of Ga, which could be due to some Ga being drawn out and oxidized when exposed to air giving a slightly smaller EDX-signal when examining the single nanoparticles with a STEM-probe oriented at their center. This is expected due to the preparation of the samples in air before the microscopy.

The STEM and EDX shows a general picture of a very mixed alloy with a broad representation of differently composed nanoparticles. As microscopy is always at risk of being statistically insignificant due to the size of the probed sample, *in situ* X-ray diffraction of the catalysts has been performed during formation, reaction and finally exposure to ambient air. Fig. 4 shows the final diffractograms after these treatments. Here the FCC crystal-pattern shows clearly on both samples agreeing with the observed fringes from the HR-TEM. The intensity difference between the samples matches the difference in mass of the Co, Cu and Ga showing that the diffracted X-rays are coming from these materials. As the  $\text{SiO}_2$  is amorphous, it does not produce significant diffraction peaks within the measured angle-interval. The changes across different treatments are only visually visible for the 17.8 wt% catalyst, which comes partly from the fact that the 3.5 wt% already after formation has a noticeably segregated alloy as the STEM-EDX in Fig. 3 showed, and that the intensity of the diffraction pattern is significantly lower.

Looking at the diffractograms of the 17.8 wt% catalyst, there is a substantial progression of the crystal from formation over reaction and into air exposure. For the (111) diffraction-peak of the 17.8 wt% catalyst, in the cut-out of Fig. 4 from  $42^\circ$  to  $45^\circ$   $2\theta$ , the peak is skewed with a main intensity at just above  $43^\circ$  and broadening towards higher angles. This skewness from the freshly formed nanoparticles show that the diffraction pattern is produced by an ensemble of closely but differently sized crystal-cells. It is seen that the overall intensity drops and the shoulder towards higher angles increases relatively to the main intensity. By using reference-lines for different Cu-Ga and Co-Ga alloys in Fig. 4, it is seen that the main-intensity can be attributed to a Cu-rich or ternary alloy, where the shoulder is associated with Co- and Co-Ga segregation. The main intensity never unifies with the reference of pure Cu-FCC, which must be caused by residing Ga. As there is no  $\text{CoCu}_2\text{Ga}$  or any similar ternary alloy in any experimental database at the time of writing, only a guess can be made towards where the ternary alloy might lie in the diffraction pattern. Cu forms in an FCC and Co in either FCC or HCP, and when alloyed with Ga both form in an FCC if the Ga-concentration is not too high (in which case a BCC is produced). This behavior is seen in the ternary  $\text{X}_2\text{YZ}$  Heusler intermetallics, which depending on relative concentrations form in a BCC-like Heusler (or  $\text{L}_{21}$  structure type) or FCC-like  $\gamma$ -Heusler (or  $\text{LiPd}_2\text{Tl}$  structure type), exactly what was found with a material-wise similar  $\text{Ni}_2\text{FeGa/SiO}_2$  catalyst [59]. This argument establishes that the observed main-intensity of the FCC-crystal structure in Fig. 4 coincides with mixed ternary alloyed  $\text{CoCu}_2\text{Ga}$  nanoparticles.

The exposure to air also seems to impact the nanoparticles of the 17.8 wt% catalyst much more than the 3.5 wt%. Composition-wise these nanoparticles are similar as of the STEM-EDX analysis, but the crystallites (shown in Fig. 4) are much larger in the 17.8 wt% and so it is speculated that the surface and not the bulk keeps the stability of the alloyed nanoparticles in oxidizing conditions eg., oxidizing conditions create a change in what is most favorable at the surface resultantly being oxidized Ga, which makes the bulk less stable and cause the shrinkage and breaking of the nanoparticles in the 17.8 wt%.

### 3.4. Formation of the catalyst and stability during reaction conditions by *in situ* characterization

Using *in situ* XRD under controlled temperature and atmosphere, the crystal phases of the ternary catalyst samples could be followed. Fig. 4 shows the diffraction patterns recorded between formation, reaction and exposure to ambient air. From Section 3.3, it has been found that the nanoparticles do form a ternary alloy of Cu, Co and Ga, although the relative concentrations vary from particle to particle. Based on this

knowledge, a simple fitting-model for the diffraction pattern was conceived so the phases of the catalysts could be followed more quantitatively during formation in  $\text{H}_2$  and reaction in  $\text{H}_2$  and CO. For the 3.5 wt% catalyst, only a mono-atomic FCC was used, and for 17.8 wt% the pattern is resolved enough to split it into a Cu-rich FCC, Co-rich FCC and Ga-rich BCC. This model is likely to be a simplification of the real ensemble of crystal structures, but it allows for a skewed FCC as well as an additional skewness to the (111) peak. Adding more patterns to the model will decrease the quality of the fit by over-fitting. Specifics of the model is described in Section 2 (*in situ* XRD) and in SI – Specifics of the XRD fitting model.

Fig. 5 shows the intensity and crystallite size resulting from said fitting. The total intensity of the 3.5 wt% and 17.8 wt% in Fig. 5 A follows an identical development: increasing during formation, stable during reaction until above  $250^\circ\text{C}$ , where it drops notably. For the individual patterns within the 17.8 wt% catalyst, it is seen that the decrease in intensity is due to a loss of the Cu-rich FCC, whereas the Co-rich FCC has a small gain. This is the same as has been observed visually in Fig. 4 that the peak-shoulder increases. At the same time, there is a small increase of the crystallite size of the Co-rich FCC, shown in Fig. 5B. All this agree well with the conceived idea that the ternary alloy segregates by smaller Co-rich particles leaving the larger Cu-rich nanoparticles. The fact that Co leaves the matrix is due to the strong interaction between Co and CO; Co can form both stable carbonyls and carbonate under ambient conditions [60]. The Cu-rich crystallites do not show any change in the data, which is because the relative change is so small that the fitting becomes insensitive to it: the crystallite size is of 30–35 nm, and the variation (noise) from fitting individual patterns are of a few nm for the Cu-rich FCC.

Using *in situ* XRD during formation and reaction has revealed macroscopic data for the progression of the catalyst which agrees with the observations of the performed microscopy. To ratify that a substantial phase separation occurs for both catalysts when exposed to reaction conditions, *in situ* XAS has been performed following the progression of each individual species. Each of three component metal edges was measured for both 3.5 wt% and 17.8 wt%  $\text{CoCu}_2\text{Ga/SiO}_2$  along with two experiments of 17.8 wt%  $\text{CoGa/SiO}_2$  and  $\text{CuGa/SiO}_2$  as reference samples. Using linear-combination-fitting of the XANES, however a crude method when applying bulk-standards to supported nanoparticles, the course of reducing the different metals could be followed. During reduction in  $\text{H}_2$  at  $620^\circ\text{C}$  of the supported CoGa and CuGa, it has been found that the most easily reduced elemental species follow as  $\text{Cu} > \text{Co} > \text{Ga}_{\text{Co}} > \text{Ga}_{\text{Cu}}$ , with the subscript showing the co-alloying element. In the 3.5 wt%  $\text{CoCu}_2\text{Ga/SiO}_2$  and the 17.8 wt%  $\text{CuGa/SiO}_2$ , Ga does not reduce completely over the course of the hydrogen-treatment. Three factors determine this sequence: the stability of the respective oxides, Gallium being energetically more favored to alloy with Co rather than Cu, and that metallic Co is more reactive and catalytically better at splitting  $\text{H}_2$  than Cu (catalyzing the reduction of Ga therefor). The higher alloying ability of Co to Ga compared to Cu explains why a small Ga-enrichment is seen from the STEM-EDX of the 3.5 wt% as shown in Fig. 3D: Ga follows Co. For further discussion of the XANES see the SI – XAS of reference  $\text{CoGa/SiO}_2$  and  $\text{CuGa/SiO}_2$  samples, SI – XAS of  $\text{CoCu}_2\text{Ga/SiO}_2$  and Figures S10-S22.

The *in-situ* XAS performed of the 3.5 wt% and 17.8 wt%  $\text{CoCu}_2\text{Ga/SiO}_2$  was done capturing both the formation of the alloy in  $\text{H}_2$  and during the exposure to CO and  $\text{H}_2$ . The EXAFS data are shown in Fig. 6. Both Co, Cu and Ga show corresponding intensity at just above  $2 \text{ \AA}$ , which arise from the nearest neighbor in the metallic alloyed phase (as the EXAFS is not phase-corrected, the resulting intensity will appear at a shorter distance than the inter-atomic coordination of  $\sim 2.5 \text{ \AA}$  as the XRD would suggest [61]). Additionally, Ga show prominent coordination below  $2 \text{ \AA}$  coming from oxidized Ga, the intermediate state between the nitrate and the final alloyed metallic state. The ratio between metallic and oxidic Ga reverses from 17.8 wt% to the 3.5 wt% catalyst. As XANES showed, the 3.5 wt% catalyst still has gallium oxide present after the



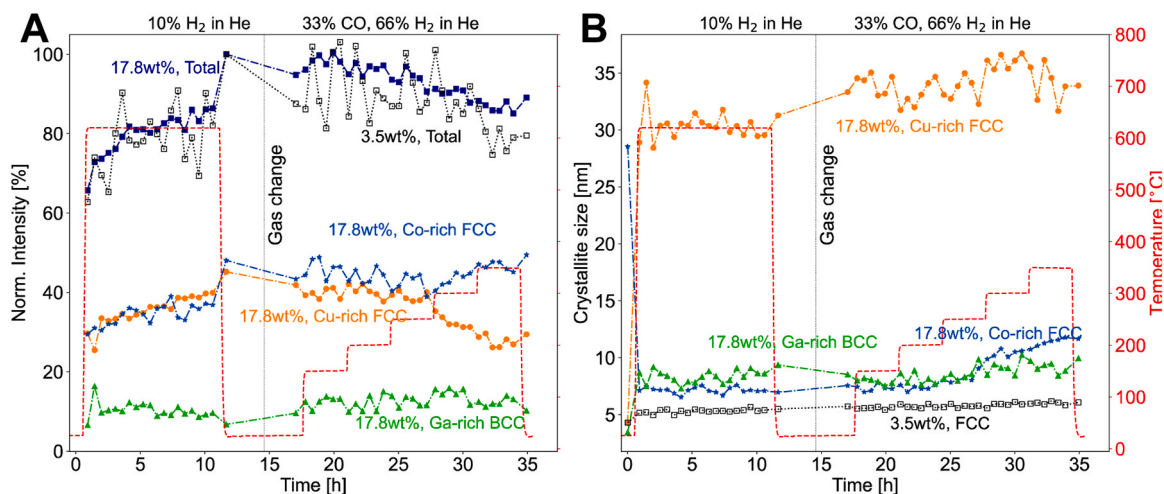


Fig. 5. in situ XRD of CoCu<sub>2</sub>Ga/SiO<sub>2</sub> during reduction and reaction conditions at 1000–1040 mbar. Graphs are showing time-resolved results of the XRD-pattern peak-fitting, using a FCC-pattern for the 3.5 wt% of CoCu<sub>2</sub>Ga/SiO<sub>2</sub>, and Cu-rich FCC, Co-rich FCC and Ga-rich BCC for the 17.8 wt% CoCu<sub>2</sub>Ga/SiO<sub>2</sub>. (A): intensity of the diffraction patterns, normalized to XRD pattern acquired at room-temperature after the reduction (after 12 hours). (B): Average crystallite-diameter extracted using the Scherrer equation [53] assuming no strain. Broadening arising from the instrument is accounted for.

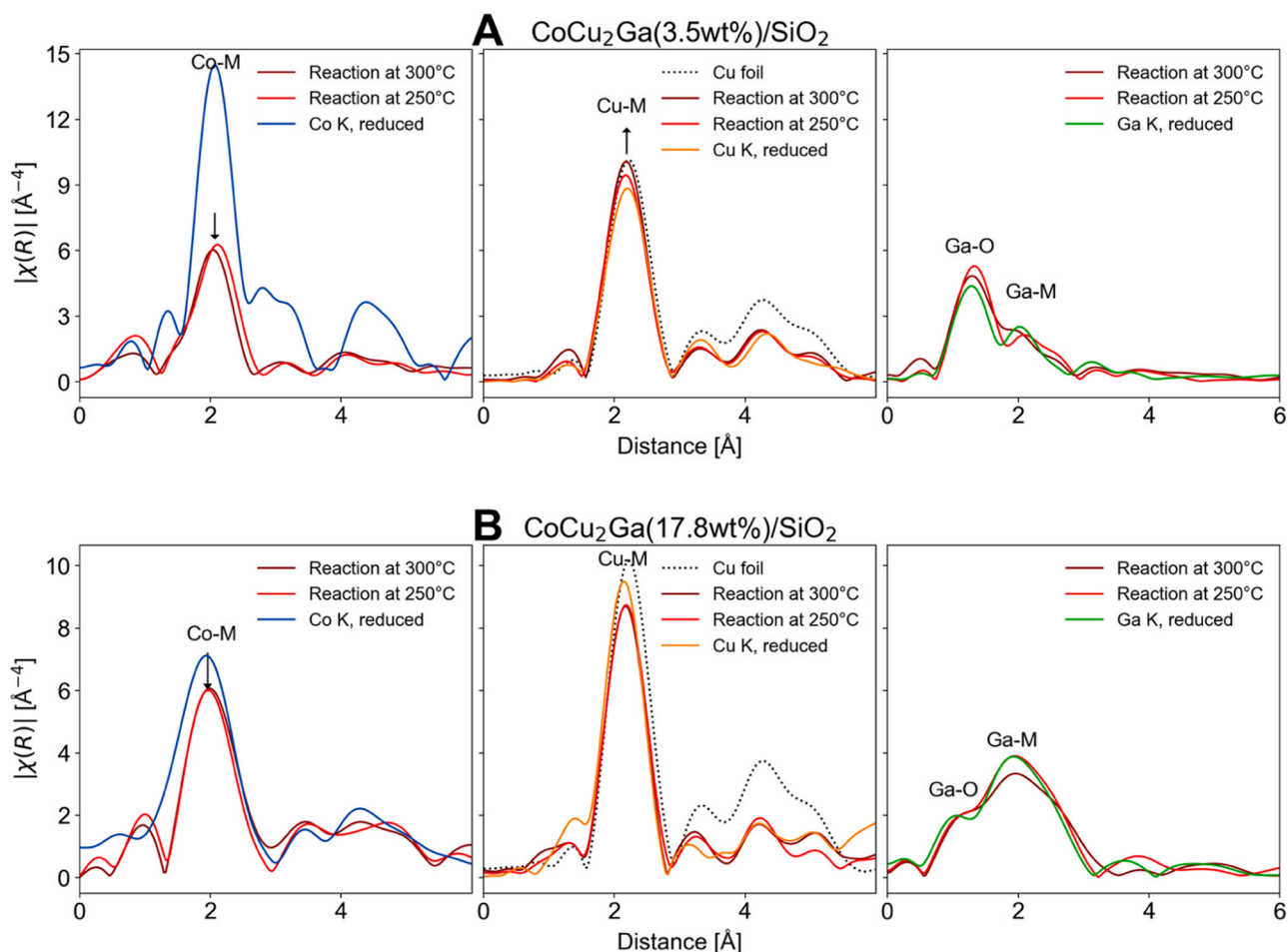


Fig. 6. k<sup>3</sup>-weighted real space EXAFS data of the 3.5 wt% and 17.8 wt% CoCu<sub>2</sub>Ga/SiO<sub>2</sub> acquired at 200 °C, after being reduced at 1 bar H<sub>2</sub> at 620 °C, and after being exposed to reaction conditions at 2 bar and the denoted temperature. For the Fourier-transform, a k-range of 3–10 Å<sup>-1</sup> was used for the Co K and Cu K, whereas 3–9 Å<sup>-1</sup> was used for the Ga K due to limitations in the beamline optics. Corresponding k<sup>2</sup>χ(k) are shown in Figs. S23–S25.

hydrogen-treatment. It may very well be that the lower surface-concentration of Cu and Co in the 3.5 wt% catalyst is not capable of reducing the rest of the gallium due to distance between

metallic particles and the residing gallium oxide.

Exposing the catalysts to reaction conditions induce notable changes to the EXAFS. The number of nearest neighbor coordination of Co goes



down for both catalyst samples, as indicated by arrows on Fig. 6. The Cu-edge change to resemble the Cu-foil. Both changes to the EXAFS certainly indicate that a phase-separation occurs by Co leaving the Cu-rich alloy, which is in line with the *in situ* XRD and STEM-EDX. The 3.5 wt% experience a much more substantial decrease in coordination of the Co than the 17.8 wt%, which is due to the difference in particle-size and the surface-area, therefore also the amount of Co exposed to the gaseous phase. The gallium-edges only show very subtle change (owing to the lower resolution of this edge).

#### 4. Discussion

Returning to the catalytic results presented in Section 3.1 and especially Fig. 1C, it was observed that the catalysts were similar in activity when comparing their formation rate for methane, but different comparing their formation of alcohol: 3.5 wt% CoCu<sub>2</sub>Ga making ethanol and methanol, and 17.8 wt% making more methanol. The *in situ* characterization gives indications on the morphology that could explain these differences in the catalytic properties: 1) the size of the nanoparticles and 2) the chemical state of the individual species.

Following 1), by XRD it was found that the 17.8 wt% have crystallites of sizes between 10 and 30 nm, whereas the 3.5 wt% features ~6 nm crystallites. Assuming a cubo-octahedron (FCC nanoparticle with only the facets of (111) and (100) exposed), a 6 nm nanoparticle would feature 70% (111), 15% (100), 13% edges and 2% corners, and approaching 30 nm you get to the asymptotic distribution of 80%/20% between (111) and (100) [57]; this means the 3.5 wt% features a magnitude or so more undercoordinated sites compared to the 17.8 wt%, and in turn giving the 3.5 wt% catalyst a magnitude higher formation rate for ethanol (assuming ethanol is only formed on edges/corners). Even if Cu-Co sites are featured on the facets, they might still selectively produce methanol, as only the undercoordinated sites have been predicted to be very selective towards ethanol [35].

Following 2), as 3.5 wt% has a larger quantity of Ga being oxidized, the alloyed nanoparticles will have a Ga-deficiency. The fact that Ga is known on several occasions to mitigate the reactivity of Co, making it less prone to CO-dissociation and Fischer-Tropsch, and more selective towards methanol [31,32,43,62], this will enforce the difference between the 17.8 wt% and 3.5 wt% catalysts. As reducible oxides on the interface of Fischer-Tropsch catalysts are known to increase the formation of oxygenates [22,33,63], it might be unexpected that the 3.5 wt% catalyst is not the more alcohol-selective catalyst despite having more partially oxidized Ga. Probably the nanoparticle-surface is much more catalytically active, and therefore more important for the measured selectivity than slightly higher presence of galliumoxide. The reason why the methane-formation rates are corresponding is that at higher temperatures, the facets become reactive enough to dissociate CO, which in turn lowers the formation of alcohol in general.

From Section 3.2, it was found that the methane- and ethanol-formation decreased on repetition of the catalytic temperature-cycle and even more so when reduced anew. The methanol-formation is more stable, and for the 17.8 wt% it was actually improved. This is caused by the phase-separation, where the catalytic ternary nanoparticles change into largely Cu and CoGa particles, both expected to be more selective towards methanol following the argument in the previous paragraph. These results indicate the need for *in situ* characterization under relevant conditions, as desired alloys such as the CoCu-alloy will undergo change which is not else observed from the initial fresh catalyst. The question is not only, how to form an “from nature energetically undesirable” CoCu-alloy, but how to keep it intact during a catalytic reaction with a gaseous specie that interacts so strongly with one and not the other. We believe that often this issue is not attended to, when claiming a successfully synthesized catalyst that produce high-order alcohols in the absence of meaning stability tests.

#### 5. Conclusion

Alloyed CoCu<sub>2</sub>Ga nanoparticles supported on SiO<sub>2</sub> with four different weight-loadings of CoCu<sub>2</sub>Ga were synthesized in this work and tested for the catalytic ability towards carbon monoxide hydrogenation at close-to-zero conversion. Here, the 3.5 wt% achieved the highest selectivity towards ethanol of 8% at 275°C and 2 bar absolute pressure, whereas the 17.8 wt% sample, being the next in regard to weight-loading, did not produce any noticeable ethanol. These two underwent characterization using STEM-EDX, both of freshly prepared and of spent samples. *In situ* XRD and *in situ* EXAFS were performed on precursor samples, following both the formation of the catalytic alloy and the changes during reaction conditions. Cycling the temperature up and down showed difference to the catalysts, in general decreasing the overall activity, although methanol-yield was less affected than methane and ethanol.

It was found with the characterization that: 1) by STEM-EDX, the alloyed nanoparticles were certainly ternary alloyed of Co, Cu and Ga, although the nanoparticles particles were not homogenous, with a deficit of Cu in small particles and deficit of Co in larger particles, and an overall small deficit of Ga in general; 2) by *in situ* XRD, that crystalline phases of FCC formed matching the nanoparticles captured by TEM, although the peak-shape in the XRD also showed that an ensemble of different crystal-structures of Cu-rich, Co-rich and Ga-rich are present in the samples; 3) by *in situ* XRD, that heating in reaction conditions above 200°C eliminated intensity from the Cu-rich crystalline phase, whereas the Co-rich crystalline phase increased in intensity as well as in crystallite-sizes; 4) by *in situ* EXAFS, that imposing reaction-condition markedly decreases the coordination of Co, that Cu-coordination increases slightly through the course of the experiments, and that Ga features atomic-coordination with Oxygen atoms both after preparation of the catalyst in hydrogen and in reaction conditions.

From above results, it has been concluded that Co and Cu, even though thermodynamically difficult to alloy, do alloy in this specific case and possibly in general will alloy easier when featuring nano-structured morphology such as nanoparticles [40,41]. To ease the alloying, Ga was included as a third constituent, although the exact role of Ga concerning stability and catalysis after the formation of the nanoparticles is unknown at this point. During reaction, there are very clear indications that Co travels to the surface, and Co/Co-Ga particles segregates out of the larger ternary nanoparticles, leaving large Cu-rich particles and small Co-rich particles. We believe the catalytic surface features Co-Cu sites, which are responsible for the observed ethanol, especially since the observed phase-segregation diminished the ethanol selectivity.

The importance of this work does not lie in the specific produced catalyst of CoCu<sub>2</sub>Ga/SiO<sub>2</sub>, which is not very competitive and could have been improved in some obvious way, eg. promotion with K to increase the reactivity of the relatively large amount of Cu on the catalyst. However, the materials knowledge presented in this work through operando studies is important considering the number of different CoCu-alloyed catalysts presented in literature used predominantly in CO-rich heated conditions for a prolonged period [24,31,32,40–46,64–66]. Especially considering that the observed phase-separation is causing an irreversible structural change for the catalyst while it is in the reactor. This ought to be a concern for the field of Co-Cu alloyed catalysts.

#### CRedit authorship contribution statement

**Anna Zimina:** Writing – review & editing, Investigation, Data curation. **Mads Lützen:** Writing – review & editing, Investigation, Formal analysis, Data curation. **Thomas Smitshuysen:** Writing – review & editing, Writing – original draft, Investigation, Formal analysis, Data curation, Conceptualization. **Christian Danvad Damsgaard:** Writing – review & editing, Supervision, Project administration, Methodology, Investigation, Funding acquisition, Formal analysis, Data curation,

Conceptualization. **Ib Chorkendorff**: Writing – review & editing, Supervision, Project administration, Funding acquisition, Conceptualization. **Helene Hagemann Jakobsen**: Writing – review & editing, Investigation, Formal analysis, Data curation, Conceptualization. **Thomas L. Sheppard**: Writing – review & editing, Investigation, Data curation.

### Declaration of Competing Interest

The authors declare that they have no known competing financial interests or personal relationships that could have appeared to influence the work reported in this paper.

### Data availability

Data will be made available on request.

### Acknowledgements

The A.P. Møller and Chastine Mc-Kinney Møller Foundation is gratefully acknowledged for the contribution towards the establishment of the Center for Electron Nanoscopy in the Technical University of Denmark.

We would like to thank the Institute for Beam Physics and Technology (IBPT) for the operation of the storage ring, the Karlsruhe Research Accelerator (KARA). We acknowledge the KIT light source for provision of instruments at the CAT-ACT beamline of the Institute of Catalysis Research and Technology (IKFT).

This work was supported by a research grant (9455) from VILLUM FONDEN.

### Compliance with ethical standards

All authors declare no conflicts of interest.

### Appendix A. Supporting information

Supplementary data associated with this article can be found in the online version at [doi:10.1016/j.apcata.2024.119636](https://doi.org/10.1016/j.apcata.2024.119636).

### References

- [1] R. Pidcock, R. McSweeney, Mapped: how climate change affects extreme eather around the World, Carbon - Clear Clim. (2021). (<https://www.carbonbrief.org/mapped-how-climate-change-affects-extreme-weather-around-the-world>).
- [2] D.J. Rasmussen, K. Bittermann, M.K. Buchanan, S. Kulp, B.H. Strauss, R.E. Kopp, M. Oppenheimer, Extreme sea level implications of 1.5 °C, 2.0 °C, and 2.5 °C temperature stabilization targets in the 21st and 22nd centuries, Environ. Res. Lett. 13 (2018).
- [3] P. Friedlingstein, M.W. Jones, M. O'Sullivan, R.M. Andrew, J. Hauck, G.P. Peters, W. Peters, J. Pongratz, S. Sitch, C. Le Quéré, D.C.E. Bakker, J.G. Canadell, P. Ciais, R.B. Jackson, P. Anthoni, L. Barbero, A. Bastos, V. Bastrikov, M. Becker, L. Bopp, E. Buitenhuis, N. Chandra, F. Chevallier, L.P. Chini, K.I. Currie, R.A. Feely, M. Gehlen, D. Gilfillan, T. Gkritzalis, D.S. Goll, N. Gruber, S. Gutekunst, I. Harris, V. Haverd, R.A. Houghton, G. Hurtt, T. Ilyina, A.K. Jain, E. Joetzjer, J.O. Kaplan, E. Kato, K.K. Goldewijk, J.I. Korsbakken, P. Landschützer, S.K. Lauvset, N. Lefevre, A. Lenton, S. Lienert, D. Lombardozi, G. Marland, P.C. McGuire, J.R. Melton, N. Metz, D.R. Munro, J.E.M.S. Nabel, S.-I. Nakaoka, C. Neill, A.M. Omar, T. Ono, A. Peregón, D. Pierrot, B. Poulter, G. Rehder, L. Resplandy, E. Robertson, C. Rödenbeck, R. Séférian, J. Schwinger, N. Smith, P.P. Tans, H. Tian, B. Tilbrook, F.N. Tubiello, G.R. van der Werf, A.J. Wiltshire, S. Zaehle, Global carbon budget 2019, Earth Syst. Sci. Data 11 (2019) 1783–1838, <https://doi.org/10.5194/essd-11-1783-2019>.
- [4] J. Hansen, M. Sato, P. Kharecha, K. Von Schuckmann, D.J. Beerling, Young people's burden: requirement of negative CO<sub>2</sub> emissions, Earth Syst. Dyn. 8 (2017) 577–616.
- [5] W.S. Broecker, Climatic change: are we on the brink of a pronounced global warming? Science (1979) 189 (4201) (1975) 460–463.
- [6] C.P. Morice, J.J. Kennedy, N.A. Rayner, P.D. Jones, Quantifying uncertainties in global and regional temperature change using an ensemble of observational estimates: the HadCRUT4 Data Set, J. Geophys Res 117 (D8101) (2012), <https://doi.org/10.1029/2011JD017187>.
- [7] R.E. Smalley, Future global energy prosperity: the terawatt challenge, MRS Bull. 30 (6) (2005) 412–417, <https://doi.org/10.1557/mrs2005.124>.
- [8] S.R. Kurtz, A.M. Leilaouioun, R.R. King, I.M. Peters, M.J. Heben, W.K. Metzger, N. M. Haegel, Revisiting the terawatt challenge, MRS Bull. 45 (3) (2020) 159–164, <https://doi.org/10.1557/mrs.2020.73>.
- [9] C.F. Shih, T. Zhang, J. Li, C. Bai, Powering the future with liquid sunshine, Joule 2 (10) (2018) 1925–1949, <https://doi.org/10.1016/j.joule.2018.08.016>.
- [10] J.E. Logsdon, Ethanol. Kirk-Othmer Encyclopedia of Chemical Technology, John Wiley & Sons, 2004, <https://doi.org/10.1002/0471238961>.
- [11] Renewable Fuels Association. Annual Ethanol Production. (<https://ethanolrfa.org/markets-and-statistics/annual-ethanol-production>) (accessed 2023-05-21).
- [12] H.T. Luk, C. Mondelli, D.C. Ferré, J.A. Stewart, J. Pérez-Ramírez, Status and prospects in higher alcohols synthesis from syngas, Chem. Soc. Rev. 46 (5) (2017) 1358–1426, <https://doi.org/10.1039/c6cs00324a>.
- [13] P. Mäki-Arvela, A. Aho, I. Simakova, D. Yu. Murzin, Sustainable aviation fuel from syngas through higher alcohols. ChemCatChem, John Wiley and Sons Inc, 2022, <https://doi.org/10.1002/cctc.202201005>.
- [14] S. Zhang, Z. Wu, X. Liu, K. Hua, Z. Shao, B. Wei, C. Huang, H. Wang, Y. Sun, A short review of recent advances in direct CO<sub>2</sub> hydrogenation to alcohols, Top. Catal. (No. 0123456789) (2021), <https://doi.org/10.1007/s11244-020-01405-w>.
- [15] A.H.M. da Silva, L.H. Vieira, C.S. Santanta, M.T.M. Koper, E.M. Assaf, J.M. Assaf, J. F. Gomes, Ethanol formation from CO<sub>2</sub> hydrogenation at atmospheric pressure using Cu catalysts: water as a key component, Appl. Catal. B 324 (2023), <https://doi.org/10.1016/j.apcatb.2022.122221>.
- [16] L. Wang, L. Wang, J. Zhang, X. Liu, H. Wang, W. Zhang, Q. Yang, J. Ma, X. Dong, S. J. Yoo, J. Kim, X. Meng, F. Xiao, Selective hydrogenation of CO<sub>2</sub> to ethanol over cobalt catalysts, Angew. Chem. Int. Ed. 57 (2018) 6104–6108, <https://doi.org/10.1002/anie.201800729>.
- [17] M. Schumann, M.R. Nielsen, T.E.L. Smits huysen, T.W. Hansen, C.D. Damsgaard, A.-C.A. Yang, M. Cargnello, J.-D. Grunwaldt, A.D. Jensen, J.M. Christensen, Rationalizing an Unexpected Structure sensitivity in heterogeneous catalysis—CO hydrogenation over Rh as a case study, ACS Catal. (2021) 5189–5201, <https://doi.org/10.1021/acscatal.0c05002>.
- [18] Z. Shao, X. Liu, S. Zhang, H. Wang, Y. Sun, CO Hydrogenation to ethanol over supported Rh-based catalyst: effect of the support, Acta Phys. Chim. Sin. 37 (10) (2021) 1911053, <https://doi.org/10.3866/PKU.WHXB201911053>.
- [19] M. Schumann, J.D. Grunwaldt, A.D. Jensen, J.M. Christensen, Investigations of mechanism, surface species and support effects in CO hydrogenation over Rh, J. Catal. 414 (2022) 90–100, <https://doi.org/10.1016/j.jcat.2022.08.031>.
- [20] A.S. Asundi, A.S. Hoffman, P. Bothra, A. Boubnov, F.D. Vila, N. Yang, J.A. Singh, L. Zeng, J.A. Raiford, F. Abild-Pedersen, S.R. Bare, S.F. Bent, Understanding structure–property relationships of MoO<sub>3</sub>-promoted Rh catalysts for syngas conversion to alcohols, J. Am. Chem. Soc. 141 (50) (2019) 19655–19668, <https://doi.org/10.1021/jacs.9b07460>.
- [21] F. Xue, W. Chen, X. Song, X. Cheng, Y. Ding, Promotional effects of Cr and Fe on Rh/SiO<sub>2</sub> catalyst for the preparation of ethanol from CO hydrogenation, RSC Adv. 6 (42) (2016) 35348–35353, <https://doi.org/10.1039/c5ra28075c>.
- [22] N.D. Subramanian, J. Gao, X. Mo, J.G. Goodwin, W. Torres, J.J. Spivey, La and/or V oxide promoted Rh/SiO<sub>2</sub> catalysts: effect of temperature, H<sub>2</sub>/CO ratio, space velocity, and pressure on ethanol selectivity from syngas, J. Catal. 272 (2) (2010) 204–209, <https://doi.org/10.1016/j.jcat.2010.03.019>.
- [23] J.A. Sibiñia, J.M. Dominguez, R.G. Herman, K. Klier, Alcohol synthesis over Fe/Cu/ZnO catalysts, Abstr. Pap. Am. Chem. Soc. 188 (August) (1984) 261–268.
- [24] X. Mo, Y.T. Tsai, J. Gao, D. Mao, J.G. Goodwin, Effect of component interaction on the activity of Co/CuZnO for CO hydrogenation, J. Catal. 285 (1) (2012) 208–215, <https://doi.org/10.1016/j.jcat.2011.09.033>.
- [25] P. Courty, D. Durand, E. Freund, A. Sugier, C1-C6 Alcohols from Synthesis Gas on Copper-Cobalt Catalysts, J. Mol. Catal. 17 (2–3) (1982) 241–254, [https://doi.org/10.1016/0304-5102\(82\)85035-9](https://doi.org/10.1016/0304-5102(82)85035-9).
- [26] E. Heracléous, E.T. Liakakou, A.A. Lappas, A.A. Lemonidou, Investigation of K-promoted Cu-Zn-Al, Cu-X-Al and Cu-Zn-X (X = Cr, Mn) catalysts for carbon monoxide hydrogenation to higher alcohols, Appl. Catal. A Gen. 455 (2013) 145–154, <https://doi.org/10.1016/j.apcata.2013.02.001>.
- [27] M. Maack, H. Friis-jensen, S. Sckerl, J.H. Larsen, I. Chorkendorff, Methanol synthesis on potassium-modified Cu (100) from CO+H<sub>2</sub> and CO+CO<sub>2</sub>+H<sub>2</sub>, Top. Catal. 22 (2003).
- [28] M. Xu, E. Iglesia, Carbon-carbon bond formation pathways in CO hydrogenation to higher alcohols, J. Catal. 188 (1) (1999) 125–131, <https://doi.org/10.1006/jcat.1999.2650>.
- [29] P.K. Frolich, W.K. Lewis, Synthesis of alcohols higher than methanol from carbon monoxide and hydrogen, Ind. Eng. Chem. 20 (4) (1928) 354–359, <https://doi.org/10.1021/ie50220a011>.
- [30] Bao, Z.; Xiao, K.; Qi, X.; Wang, X.; Zhong, L.; Fang, K.; Lin, M.; Sun, Y. Higher Alcohol Synthesis over Cu-Fe Composite Oxides with High Selectivity to C<sub>2</sub>+ OH; 2013; Vol. 22.
- [31] X. Ning, Z. An, J. He, Remarkably efficient CoGa catalyst with uniformly dispersed and trapped structure for ethanol and higher alcohol synthesis from syngas, J. Catal. 340 (2016) 236–247, <https://doi.org/10.1016/j.jcat.2016.05.014>.
- [32] Z. An, X. Ning, J. He, Ga-promoted CO insertion and C–C coupling on Co catalysts for the synthesis of ethanol and higher alcohols from syngas, J. Catal. 356 (2017) 157–164, <https://doi.org/10.1016/j.jcat.2017.09.020>.
- [33] M.K. Gnanamani, M.C. Ribeiro, W. Ma, W.D. Shafer, G. Jacobs, U.M. Graham, B. H. Davis, Fischer-tropsch synthesis: metal-support interfacial contact governs oxygenates selectivity over CeO<sub>2</sub> supported Pt-Co catalysts, Appl. Catal. A Gen. 393 (1–2) (2011) 17–23, <https://doi.org/10.1016/j.apcata.2010.11.019>.

- [34] A.J. Medford, A.C. Lausche, F. Abild-Pedersen, B. Temel, N.C. Schjødt, J. K. Nørskov, F. Studt, Activity and selectivity trends in synthesis gas conversion to higher alcohols, *Top. Catal.* 57 (1–4) (2014) 135–142, <https://doi.org/10.1007/s11244-013-0169-0>.
- [35] A. Cao, J. Schumann, T. Wang, L. Zhang, J. Xiao, P. Bothra, Y. Liu, F. Abild-Pedersen, J.K. Nørskov, Mechanistic insights into the synthesis of higher alcohols from syngas on CuCo alloys, *ACS Catal.* 8 (11) (2018) 10148–10155, <https://doi.org/10.1021/acscatal.8b01596>.
- [36] T. Nishizawa, K. Ishida, The Co-Cu (Cobalt-Copper) System, *Bull. Alloy Phase Diagr.* 5 (2) (1984) 161–165, <https://doi.org/10.1007/BF02868953>.
- [37] Q. Chen, Z. Jin, The Fe-Cu system: a thermodynamic evaluation, *Metall. Mater. Trans. A* 26 (2) (1995) 417–426, <https://doi.org/10.1007/BF02664678>.
- [38] H.T. Luk, C. Mondelli, S. Mitchell, S. Siol, J.A. Stewart, D. Curulla Ferré, J. Pérez-Ramírez, Role of carbonaceous supports and potassium promoter on higher alcohols synthesis over copper-iron catalysts, *ACS Catal.* 8 (10) (2018) 9604–9618, <https://doi.org/10.1021/acscatal.8b02714>.
- [39] H.T. Luk, C. Mondelli, S. Mitchell, D. Curulla Ferré, J.A. Stewart, J. Pérez-Ramírez, Impact of Carrier acidity on the conversion of syngas to higher alcohols over zeolite-supported copper-iron catalysts, *J. Catal.* 371 (2019) 116–125, <https://doi.org/10.1016/j.jcat.2019.01.021>.
- [40] A. Cao, G. Liu, Y. Yue, L. Zhang, Y. Liu, Nanoparticles of Cu-Co alloy derived from layered double hydroxides and their catalytic performance for higher alcohol synthesis from syngas, *RSC Adv.* 5 (72) (2015) 58801–58812, <https://doi.org/10.1039/c5ra05190h>.
- [41] G. Prieto, S. Beijer, M.L. Smith, M. He, Y. Au, Z. Wang, D.A. Bruce, K.P. De Jong, J. J. Spivey, P.E. De Jongh, Design and synthesis of copper-cobalt catalysts for the selective conversion of synthesis gas to ethanol and higher alcohols, *Angew. Chem. - Int. Ed.* 53 (25) (2014) 6397–6401, <https://doi.org/10.1002/anie.201402680>.
- [42] Y. Xiang, R. Barbosa, X. Li, N. Kruse, Ternary cobalt-copper-niobium catalysts for the selective CO hydrogenation to higher alcohols, *ACS Catal.* 5 (5) (2015) 2929–2934, <https://doi.org/10.1021/acscatal.5b00388>.
- [43] K. Sun, Y. Wu, M. Tan, L. Wang, G. Yang, M. Zhang, W. Zhang, Y. Tan, Ethanol and higher alcohols synthesis from syngas over CuCoM (M=Fe, Cr, Ga and Al) Nanoplates Derived From Hydrotalcite-Like Precursors, *ChemCatChem* 11 (11) (2019) 2695–2706, <https://doi.org/10.1002/cctc.201900096>.
- [44] Y. Xiang, V. Chitry, P. Liddicoat, P. Felfer, J. Cairney, S. Ringer, N. Kruse, Long-chain terminal alcohols through catalytic CO hydrogenation, *J. Am. Chem. Soc.* 135 (19) (2013) 7114–7117, <https://doi.org/10.1021/ja402512r>.
- [45] Y. Xiang, V. Chitry, N. Kruse, Selective catalytic CO hydrogenation to short- and long-chain C<sub>2+</sub> alcohols, *Catal. Lett.* 143 (9) (2013) 936–941, <https://doi.org/10.1007/s10562-013-1060-0>.
- [46] K. Sun, M. Tan, Y. Bai, X. Gao, P. Wang, N. Gong, T. Zhang, G. Yang, Y. Tan, Design and synthesis of spherical-plate-like ternary copper-cobalt-manganese catalysts for direct conversion of syngas to ethanol and higher alcohols, *J. Catal.* 378 (2019) 1–16, <https://doi.org/10.1016/j.jcat.2019.08.013>.
- [47] S. Kirklin, J.E. Saal, B. Meredig, A. Thompson, J.W. Doak, M. Aykol, S. Rühl, C. Wolverton, The open quantum materials database (OQMD): assessing the accuracy of DFT formation energies, *NPJ Comput. Mater.* (2015) 15010, <https://doi.org/10.1038/npjcompumats.2015.10>.
- [48] J.E. Saal, S. Kirklin, M. Aykol, B. Meredig, C. Wolverton, Materials design and discovery with high-throughput density functional theory: the open quantum materials database (OQMD), *Jom* 65 (11) (2013) 1501–1509, <https://doi.org/10.1007/s11837-013-0755-4>.
- [49] J.R. Taylor. *An Introduction to Error Analysis - The Study of Uncertainties in Physical Measurements*, second ed., University Science Books, 1996.
- [50] P. Hovington, D. Drouin, R. Gauvin, CASINO: a new monte carlo code in C language for electron beam interaction - part I: description of the program, *Scanning* 19 (1) (1997) 1–14.
- [51] J. Schindelin, I. Arganda-Carreras, E. Frise, V. Kaynig, M. Longair, T. Pietzsch, S. Preibisch, C. Rueden, S. Saalfeld, B. Schmid, J.Y. Tinevez, D.J. White, V. Hartenstein, K. Eliceiri, P. Tomancak, A. Cardona, Fiji: an open-source platform for biological-image analysis, *Nat. Methods* 9 (7) (2012) 676–682, <https://doi.org/10.1038/nmeth.2019>.
- [52] C.A. Schneider, W.S. Rasband, K.W. Eliceiri, NIH image to imageJ: 25 years of image analysis, *Nat. Methods* 9 (7) (2012) 671–675, <https://doi.org/10.1038/nmeth.2089>.
- [53] Scherrer, P. Bestimmung Der Grosse Und Der Inneren Struktur von Kolloidteilchen Mittels Röntgestrahlen. Nachrichten von der Gesellschaft der Wissenschaften zu Göttingen, Mathematisch-Physikalische Klasse 1918, No. 26. 98–100.
- [54] S.R. Sternberg, Biomedical image processing, *Computer* 16 (1) (1983) 22–34, <https://doi.org/10.1109/MC.1983.1654163>.
- [55] A. Zimina, K. Dardenne, M.A. Denecke, D.E. Doronkin, E. Huttel, H. Lichtenberg, S. Mangold, T. Pruessmann, J. Rothe, T. Spangenberg, R. Steininger, T. Vitova, H. Geckeis, J.D.C.A.T.-A.C.T.-A. Grunwaldt, New highly versatile x-Ray spectroscopy beamline for catalysis and radionuclide science at the KIT synchrotron light facility ANKA, *Rev. Sci. Instrum.* 88 (11) (2017) 113113, <https://doi.org/10.1063/1.4999928>.
- [56] B. Ravel, M. Newville, ATHENA, ARTEMIS, HEPHAESTUS: data analysis for X-Ray absorption spectroscopy using IFEFFIT, *J. Synchrotron Radiat.* 12 (4) (2005) 537–541, <https://doi.org/10.1107/S0909049505012719>.
- [57] R. Van Hardeveld, F. Hartog, The statistics of surface atoms and surface sites on metal crystals, *Surf. Sci.* 15 (2) (1969) 189–230, [https://doi.org/10.1016/0039-6028\(69\)90148-4](https://doi.org/10.1016/0039-6028(69)90148-4).
- [58] A. Belkly, M. Helderman, V.L. Karen, P. Ulkch, New developments in the inorganic crystal structure database (ICSD): accessibility in support of materials research and design, *Acta Crystallogr B* 58 (3 PART 1) (2002) 364–369, <https://doi.org/10.1107/S0108768102006948>.
- [59] T.E.L. Smits huysen, M.R. Nielsen, T. Pruessmann, A. Zimina, T.L. Sheppard, J. D. Grunwaldt, I. Chorkendorff, C.D. Damsgaard, Optimizing Ni–Fe–Ga Alloys into Ni<sub>2</sub>FeGa for the Hydrogenation of CO<sub>2</sub> into Methanol, *ChemCatChem* 12 (12) (2020) 3265–3273, <https://doi.org/10.1002/cctc.202000174>.
- [60] J.R. Rumble, D.R. Lide, B.T. J. CRC Handbook of Chemistry and Physics, 98th ed., CRC Press, 2017.
- [61] J. Als-Nielsen, D. McMorrow. *Elements of Modern X-Ray Physics*, second ed., Wiley, 2011.
- [62] J.A. Singh, A. Cao, J. Schumann, T. Wang, J.K. Nørskov, F.A. Pedersen, S.F. Bent, Theoretical and experimental studies of CoGa catalysts for the hydrogenation of CO<sub>2</sub> to methanol, *Catal. Lett.* 148 (12) (2018) 3583–3591, <https://doi.org/10.1007/s10562-018-2542-x>.
- [63] R. Burch, M.I. Fetch, Kinetic and transient kinetic investigations of the synthesis of oxygenates from carbon monoxide/hydrogen mixtures on supported rhodium catalysts, *Appl. Catal. A Gen.* 88 (1) (1992) 77–99, [https://doi.org/10.1016/0926-860X\(92\)80197-K](https://doi.org/10.1016/0926-860X(92)80197-K).
- [64] M. Ao, G.H. Pham, J. Sunarso, F. Li, Y. Jin, S. Liu, Effects of Alkali Promoters on Tri-Metallic Co-Ni-Cu-based perovskite catalyst for higher alcohol synthesis from syngas, *Catal. Today* 355 (June 2019) (2020) 26–34, <https://doi.org/10.1016/j.cattod.2019.06.061>.
- [65] L. Zhao, J. Duan, Q. Zhang, Y. Li, K. Fang, Preparation, structural characteristics, and catalytic performance of Cu-Co alloy supported on Mn-Al oxide for higher alcohol synthesis via syngas, *Ind. Eng. Chem. Res* 57 (44) (2018) 14957–14966, <https://doi.org/10.1021/acs.iecr.8b03304>.
- [66] Z. Wang, J.J. Spivey, Effect of ZrO<sub>2</sub>, Al<sub>2</sub>O<sub>3</sub> and La<sub>2</sub>O<sub>3</sub> on cobalt-copper catalysts for higher alcohols synthesis, *Appl. Catal. A Gen.* 507 (2015) 75–81, <https://doi.org/10.1016/j.apcata.2015.09.032>.